Journal of Materials Chemistry A

ROYAL SOCIETY OF CHEMISTRY

COMMUNICATION

View Article Online
View Journal | View Issue

Cite this: J. Mater. Chem. A, 2025, 13, 9055

Received 19th January 2025
Accepted 12th March 2025

DOI: 10.1039/d5ta00506j

rsc.li/materials-a

Electrochemically activated copper-based catalyst from a coordination polymer for stable hydrogen evolution reaction†

Taehun Im,‡[ae] Joo-Won Lee,‡[ab] Sung-Chul Kim,[c] Sungju Jun,[ae] Jae-Seung Lee,[e] Min-Seok Kim,[b] Jae Kyun Lee[d] and Sohee Jeong *[a]

Noble metal catalysts are highly efficient for the hydrogen evolution reaction (HER), but their scarcity and cost limit their widespread use. Copper-based materials, which are abundant and inexpensive, offer a promising alternative. However, their intrinsic limitations, such as weak hydrogen adsorption and poor stability, often restrict their catalytic performance. This study introduces a novel strategy for synthesizing a highly stable HER catalyst through the electrochemical activation of a copper-based coordination polymer. The resulting composite material exhibits a unique structure with aligned $Cu^{2+}/Cu^{+}/Cu^{0}$ active sites, which significantly enhances HER activity and long-term stability. The formation of these active sites is influenced by the sulfur-rich environment of the coordination polymers. This work provides valuable insights for developing efficient and sustainable HER catalysts using earth-abundant materials.

Introduction

Noble metals, such as Rh, Ir, and Pt, are widely recognized as ideal catalysts for the hydrogen evolution reaction (HER) due to their favorable hydrogen adsorption and desorption processes, as described by the Sabatier principle.[1–4] However, their scarcity and high cost have driven significant research efforts toward developing alternative HER catalysts using more affordable and abundant elements.[5–7] Earth-abundant copper-based materials have exhibited outstanding performances in electrocatalytic CO_2 reduction[8–10] and water splitting as photoelectrodes.[11–13] Nevertheless, copper's completely filled d-orbital configuration results in weak hydrogen interactions, limiting its HER activity.[14] To address this, researchers have introduced defect-engineered copper (*e.g.*, through strain and doping)[15,16] and copper-based compounds (such as oxides, sulfides, and phosphides),[17–19] which have shown improved HER activities. However, copper-based catalysts often degrade into metallic Cu under reducing conditions of HER, leading to a loss in catalytic activity due to the elimination of active sites.[20]

Recently, spontaneous composite formation through electrochemical processes has emerged as a promising strategy to overcome the challenges of traditional material preparation methods, such as chemical and thermal treatments, which involve harsh conditions and difficulty in controlling active sites. Electrochemical activation, in particular, allows fine-tuning of surface active sites by introducing various Cu oxidation states (Cu^0 to Cu^{2+}) and their mixtures under relatively mild conditions.[21] Copper-based composites, electrochemically derived from copper oxides (Cu_2O/Cu from Cu_2O and CuO/Cu from CuO), enable effective charge transfer because of the theoretical conduction band edge positions of Cu_2O and CuO, which are well-aligned with the hydrogen redox potential. However, most studies on these materials have focused on their use in electrocatalytic CO_2 reduction.[22,23]

Experimentally, a study utilizing Cu_9S_5 nanocrystals as a precursor for the *in situ* electrochemical conversion into Cu_2O/Cu achieved a low overpotential of −120 mV at −10 mA cm^{-2} for HER.[24] However, the electrocatalytic stability of this structure remains insufficiently explored. Recently, copper-based coordination polymers (CPs) have emerged as promising precursors for efficient catalysts due to their flexibility in modifying their coordination geometry.[25–27] Nevertheless, CP-derived copper-based catalysts tend to be converted into metallic Cu during

[a]Materials Architecturing Research Center, Korea Institute of Science and Technology, 5, Hwarang-ro 14 gil, Seongbuk-gu, Seoul, 02792, Republic of Korea. E-mail: soheejeong@kist.re.kr

[b]Extreme Materials Research Center, Korea Institute of Science and Technology, 5, Hwarang-ro 14 gil, Seongbuk-gu, Seoul, 02792, Republic of Korea

[c]Advanced Analysis and Data Center, Korea Institute of Science and Technology, 5, Hwarang-ro 14 gil, Seongbuk-gu, Seoul, 02792, Republic of Korea

[d]Brain Science Institute, Korea Institute of Science and Technology, 5, Hwarang-ro 14 gil, Seongbuk-gu, Seoul, 02792, Republic of Korea

[e]Department of Materials Science and Engineering, Korea University, 145, Anam-ro, Seongbuk-gu, Seoul, 02841, Republic of Korea

† Electronic supplementary information (ESI) available. CCDC 2417754. For ESI and crystallographic data in CIF or other electronic format see DOI: https://doi.org/10.1039/d5ta00506j

‡ These authors contributed equally to this work.

HER, as predicted by the Pourbaix diagram, which leads to the loss of initially intended active sites.

In this study, we introduce a highly stable HER catalyst based on a copper composite structure with aligned $Cu^{2+}/Cu^{+}/Cu^{0}$ active sites formed through the electrochemical activation (EA) of a copper-based CP. Synthesized *via* a simple method, a copper-based CP transforms under electrochemical reduction into a (111)-aligned Cu_2O&CuO/Cu structure with $Cu^{2+}/Cu^{+}/Cu^{0}$ active sites on the surface. These sites exhibited significantly enhanced HER activity and exceptional durability exceeding three months, outperforming copper-based materials prepared through chemical activation (CA) and thermal activation (TA). Linear sweep voltammetry (LSV) and *in situ* Raman spectroscopy confirmed that the enhanced HER performance and stability (over 2800 h) arise not merely from surface oxides but from the aligned hetero-valent active sites. Notably, these unique active sites formed only when the copper-based CP featuring a sulfur-rich Cu coordination environment was used for electrochemical activation.

Experimental

Materials

Copper(II) chloride ($CuCl_2$, 97%, Sigma-Aldrich), *o*-tolylthiourea (98%, Tokyo Chemical Industry Co.), ethyl alcohol anhydrous (99.9%, Samchun Chemicals), potassium dioxide (KO_2, powder, Sigma-Aldrich), Nafion-117 solution (~5% in water, Sigma-Aldrich), platinum on carbon (Pt/C, 10 wt%, Sigma-Aldrich), copper(II) oxide (CuO, 99%, Sigma-Aldrich), copper(I) oxide (Cu_2O, 95%, Daejung), and copper nanoparticles (CuNP, 25 nm particle size, Sigma-Aldrich) were purchased and used without further purification.

Synthesis of copper-based materials

For the synthesis of TT-CP, $CuCl_2$ (0.744 mmol) and *o*-tolylthiourea (1.48 mmol) were mixed in 100 ml of ethanol solution for 10 min under vigorous stirring at room temperature. Precipitated white powders of TT-CP were washed with ethanol three times. For chemical activation, as-synthesized TT-CP powders (120 mg) were dispersed in 50 ml of deionized (DI) water under vigorous stirring, and KO_2 (4 mmol) was slowly added to the DI solution. The resulting system was heated at 90 °C and maintained for 24 hours to produce CuO from the CA process of TT-CP (CA-CuCP). Final powders of CA-CuCP were obtained after washing and filtration. For the thermal activation of TT-CP to convert into CuO (TA-CuCP), TT-CP powders were heated at 900 °C under an ambient condition for 4 h in the tube furnace. For the electrochemical activation (EA) process of TT-CP, a catalyst ink was prepared by mixing TT-CP (10 mg), Nafion-117 solution (0.120 ml), and ethanol (1.88 ml) together and deposited on glassy carbon electrodes or graphite carbon papers to be the loading mass of 0.28 mg cm^{-2}. The EA process was carried out in an Ar-saturated 0.5 M H_2SO_4 electrolyte with the chronopotentiometry measurement at the current density of −100 mA cm^{-2} for 20 h.

Materials characterization

Cu L-edge XAS measurements were conducted at the 10D KIST-PAL beamlines in the Pohang Accelerator Laboratory (PAL). X-ray photoelectron spectroscopy (XPS) results were obtained using Nexsa (ThermoFisher Scientific) instrument to investigate the chemical states. High-resolution TEM (HR-TEM) images were obtained *via* the FEI Titan 80-300 TEM instrument. Energy dispersive X-ray spectroscopy (EDS) elemental mapping results were recorded by Talos F200X TEM equipped with an extreme-field emission gun (X-FEG) and superEDX-embedded system with four silicon drift detectors (SDDs). Scanning electron microscopy (SEM) images were obtained from the FEI Inspect F SEM instrument. Powder X-ray diffraction (PXRD) patterns were measured using a D8 ADVANCE (Bruker) equipped with a Cu K-alpha radiation source. Raman spectra were recorded by a confocal Raman microscope (inVia Reflex, Renishaw) with a laser excitation wavelength of 532 nm. Fourier-transform infrared (FT-IR) spectra were obtained using a Nicolet iS50 FT-IR spectrometer (Thermo Fisher Scientific).

Electrochemical measurements

For preparing each catalyst inks, 10 mg of catalyst powders (TT-CP, TA-CuCP, CA-CuCP, CuNP, Com-CuO, Com-Cu_2O, and Pt/C), 0.120 ml of Nafion-117, and 1.88 ml of ethanol were mixed to be a concentration of 5 mg ml^{-1}. Each catalyst ink was dropped onto a glassy carbon electrode (GCE) with a diameter of 3 mm to make a catalyst loading of 0.283 mg cm^{-2}. All electrochemical measurements were carried out in the configuration of a standard three-electrode cell, where catalyst-loaded GCE, saturated calomel electrode (SCE), and graphite carbon electrodes were used as the working, reference, and counter electrodes, respectively. All measurements were operated in the acidic electrolyte (0.5 M H_2SO_4) saturated with Ar by continuously purging 99.999% Ar gas with a flow rate of 50 sccm. The potentials *versus* SCE and those *versus* RHE were transformed *via* the below equations:

$$E_{RHE} = E^{0}_{SCE} + E_{SCE} + 0.0591 \times pH$$

$$E^{0}_{SCE} = 0.241\ V\ \textit{vs.}\ RHE\ at\ 25\ ^{\circ}C$$

Linear sweep voltammetry was conducted to obtain current density (j, mA cm^{-2}) with a scan rate of 5 mV s^{-1}, and the corresponding Tafel slope was calculated by plotting $\log|j|$ with respect to overpotential.

Results and discussion

Electrochemically activated copper-based catalyst

A new copper-based coordination polymer was synthesized as a powder by simply mixing $CuCl_2$ and *o*-tolylthiourea, namely TT-CP (Fig. S1, ESI†), and then utilized as a precursor for the EA process, as shown in Fig. 1a. The structure of TT-CP was confirmed through single crystal X-ray diffraction analysis. By adjusting the reaction temperature, TT-CP could be grown as

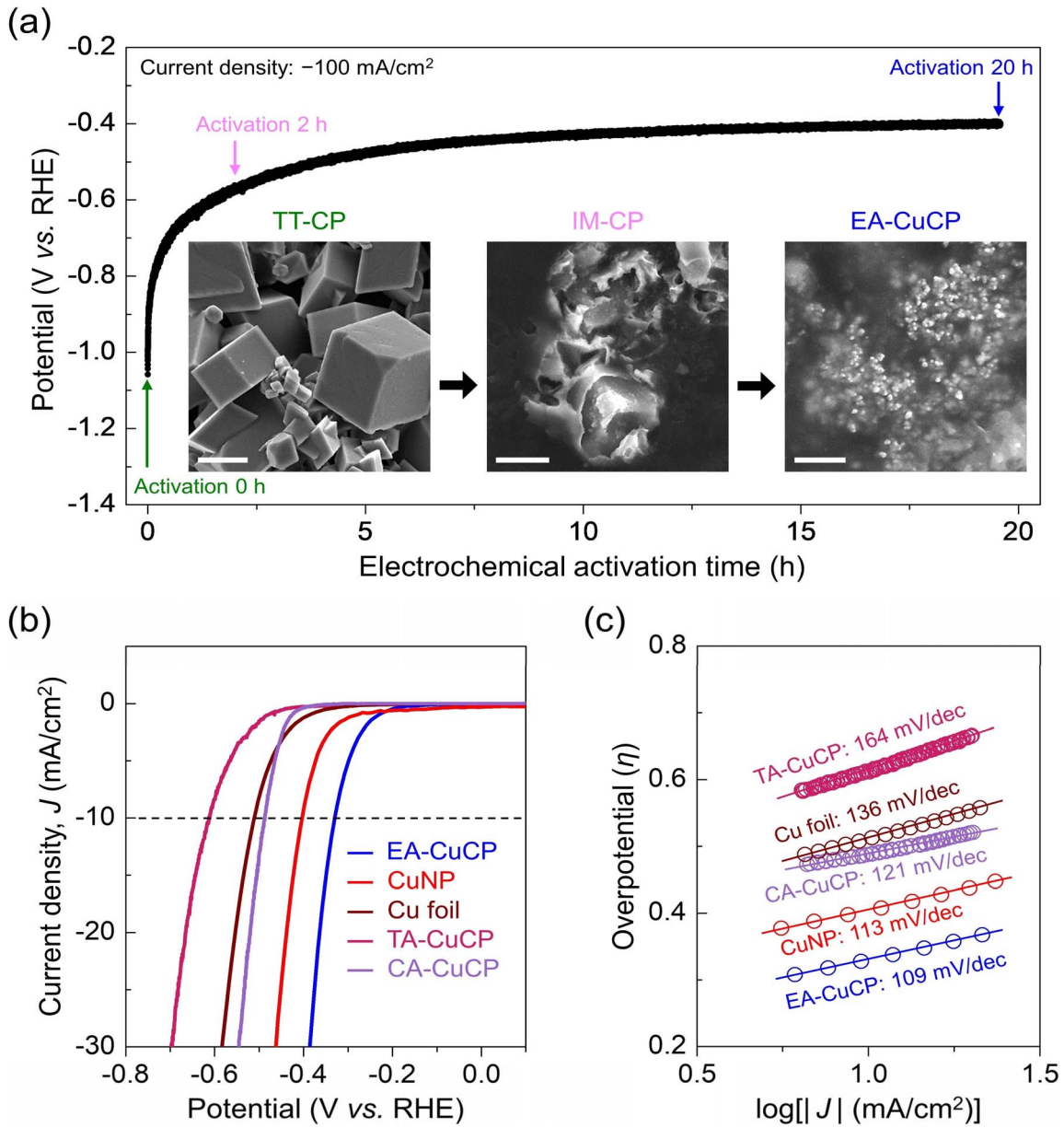

Fig. 1 HER performance of electrochemically activated copper-based catalyst. (a) Chronopotentiometry record of TT-CP under the constant current-density condition of −100 mA cm^{-2}. Inset SEM images present the morphology of TT-CP, IM-CP, and EA-CuCP with the scale bar of 10, 5, and 1 μm, respectively. (b) HER polarization curves of CA-CuCP, TA-CuCP, Cu foil, CuNP, and EA-CuCP. (c) Tafel slopes of CA-CuCP, TA-CuCP, Cu foil, CuNP, and EA-CuCP.

either a millimeter-scale single crystal (Fig. S2a, ESI†) or micrometer-scale particles (Fig. S3, ESI†). The synthesized TT-CP powder showed the same coordination structure as single crystal TT-CP (Fig. S2b, ESI†) within the allowable tolerance (Table S1, ESI†). A crystallographic information file (CIF) of TT-CP, demonstrated by single crystal X-ray diffraction, is available in ESI.† The SEM image of TT-CP (Fig. S3, ESI†) exhibits cube morphology with a diameter of *ca.* 5 μm. EDS mapping results confirmed that TT-CP is composed of Cu, S, Cl, C, and N (Fig. S3 and Table S2, ESI†). The comparison of FT-IR spectra between *o*-tolylthiourea and TT-CP (Fig. S4, ESI†) reveals the similar stretching bands of C–H, N–H, and C–N,[28] except for the change in polar structure transformation (3300–3000 cm^{-1}) and the reduced absorption signal in C=S intensity (1110–1120 cm^{-1}) arising from the Cu–S coordination formation.[29] The chemical analysis of TT-CP by XPS measurements (Fig. S5, ESI†) confirms the formation of Cu(I)–Cl structure coordinated by S atoms of *o*-tolylthiourea in TT-CP (see $Cu_4S_6Cl_4$ cluster structure in Fig. S1, ESI†) when comparing with the commercial CuCl and *o*-tolylthiourea. The C 1s, N 1s, and S 2p core-level binding energies in TT-CP are shifted toward a higher binding energy due to the electron-donating property of sulfur in thiourea derivatives,[30] confirming the Cu–S coordination bond. Single-crystal and XPS analyses confirmed that the Cu in TT-CP is coordinated with S at

a ratio of 1 : 1.5, and this TT-CP was subsequently utilized in catalyst activation.

As-synthesized TT-CP was electrochemically activated for the conversion into copper-based materials (EA-CuCP) at the constant current density of −100 mA cm^{-2}, as exhibited in Fig. 1a. Based on the Pourbaix diagram, the potential profile of EA-CuCP is sufficient to be reduced to metallic Cu because it is more negative than −0.4 V *vs.* RHE for 20 h.[31] The structural evolution from TT-CP to intermediate CP (IM-CP) and EA-CuCP was confirmed by SEM (Fig. 1a) and Raman (Fig. S6, ESI†) spectroscopy. The rapid change in potential was measured during the conversion into IM-Cu along with the emergence of metallic Cu. This observation means that Cu–S and Cu–Cl coordination bonds are broken and rapidly transformed at an early activation stage (Fig. S6, ESI†). This is also confirmed by a comparison of the HER activity of IM-CP, which is significantly increased compared to TT-CP (Fig. S7, ESI†). In addition, it collapses and turns into precipitated Cu nanoclusters. The PXRD pattern of EA-CuCP reveals that the EA-CuCP exists as metallic Cu (Fig. S8, ESI†). Interestingly, through the Raman spectrum, we found that EA-CuCP is also composed of Cu_2O and CuO (Fig. S6, ESI†) along with metallic Cu. In other words, electrochemical activation induces the composite of Cu, Cu_2O, and CuO from the coordination polymer, which does not follow the Pourbaix diagram in that unusual oxides appear.[31]

The HER activity of EA-CuCP was evaluated under an acidic condition (0.5 M H_2SO_4), compared to those of TT-CP-derived CuO (CA-CuCP and TA-CuCP) and commercial copper-based materials (Cu foil and copper nanoparticles with a diameter of 60–80 nm, CuNP). TT-CP-derived CuO was studied to investigate the influence of activation methods on HER performance. As shown in Fig. 1b, EA-CuCP exhibits the lowest overpotential (331 mV) at a current density of −10 mA cm^{-2} among the TT-CP-derived catalysts, including CA-CuCP (487 mV) and TA-CuCP (612 mV). We found that CA and TA processes converted TT-CP into only CuO, as confirmed by PXRD patterns and Raman spectra (Fig. S8 and S9, ESI†). The HER performance of EA-CuCP was also compared with bulk Cu foil and CuNP, demonstrating superiority over both (406 and 514 mV, respectively). The ECSA comparison with CuNP is shown in Fig. S10.† These results suggest that the unique structure of EA-CuCP may influence its enhanced HER activity (*vide infra*). The analysis of the Tafel slopes of copper-based materials provides insight into the rate-determining step for HER (Fig. 1c). The EA-CuCP catalyst shows the lowest Tafel slope of 109 mV dec^{-1}, accounting for its lowest overpotential. Thus, the best HER performance is confirmed in EA-CuCP. All copper-based materials show Tafel slopes ranging from 109 to 164 mV dec^{-1}, implying that the Volmer process (H^+ adsorption on the surface) is a rate-determining step.[32]

HER stability of EA-CuCP

The HER polarization curve of EA-CuCP was compared with Pt/C, as shown in Fig. S11 (ESI).† Notably, EA-CuCP shows better one-day HER stability, represented by an average potential of −0.358 V *vs.* RHE, at a current density of −10 mA cm^{-2} (Fig. 2a) compared with the Pt/C (−0.432 V *vs.* RHE). Within 5 h of the stability test, Pt/C exhibits a significant potential degradation because of its low stability under HER conditions.[33–35] In contrast, EA-CuCP shows excellent stability under the same condition, supported by the structural durability of its copper-based composite structure (Fig. S12, ESI†). In order to examine the catalytic activity and its relationship with structural stability, Tafel slopes were analyzed for both catalysts. In Fig. 2b, Pt/C exhibits a lower Tafel slope of 41 mV dec^{-1} at the $\log|J|$ region of <1.0 (current density < −10 mA cm^{-2}), consistent with its ideal interaction with adsorbed H ($\Delta G_{H^*} = -0.1$ eV).[1] However, at $\log|J| \approx 1.0$, the Tafel slope of Pt/C rises to 133 mV dec^{-1}, exceeding that of EA-CuCP (109 mV dec^{-1}), suggesting structural and catalytic instability under HER conditions. By comparison, the Tafel slopes of EA-CuCP at the $\log|J|$ region of <1.0 (96 mV dec^{-1}) and the region of 1.0 (109 mV dec^{-1}) expose less difference (Fig. 2b). These observations indicate that EA-CuCP maintains electrocatalytic stability under HER conditions, even though the interaction between adsorbed H and metallic Cu ($\Delta G_{H^*} = 0.2$ eV) differs significantly from Pt.[1] The lowest overpotential and Tafel slope of EA-CuCP among copper-based materials may be attributed to its unique composite structure (Cu, Cu_2O, and CuO) formed through the EA process of TT-CP.

To confirm the long-term HER stability, EA-CuCP was tested at a current density of −20 mA cm^{-2}. Surprisingly, catalytic performance was maintained for over 3 months, as shown in Fig. 2c, with an average potential value of −0.407 V *vs.* RHE over 2800 h of testing. During the stability test, EA-CuCP was periodically restarted to refill the electrolytes.[36] After each restart, EA-CuCP showed a recovery in potential toward a less negative voltage, possibly due to the surface structure of EA-CuCP. The Raman and XRD analyses suggest that the surface of EA-CuCP consists of Cu_2O and CuO layers surrounding a metallic Cu (Fig. S6 and S8, ESI†). It is known that H_2O molecules and sulfate ions can adsorb onto the surface of copper oxides,[37] which slightly degrades the HER overpotential. Therefore, the potential recovery of EA-CuCP after a pause in HER operation correlates with a copper-based composite structure and denotes long-term preservation of this structure. Additionally, EA-CuCP exhibits remarkable potential retention, with an average potential value of −0.507 V *vs.* RHE for 350 h at a higher current density of −200 mA cm^{-2} (Fig. 2d). To the best of our knowledge, no copper-based material has previously shown HER stability on par with the long-term performance of EA-CuCP (Table S3, ESI†).

Composite structure of EA-CuCP

A transmission electron microscopy (TEM) analysis was performed to better understand the *in situ* evolved composite structure of EA-CuCP. The resulting EA-CuCP shows an overall size of *ca.* 2 μm, containing aggregated Cu particles (Fig. 3a). The size of an individual Cu particle is around 150 nm, with its surface covered by oxygen-rich copper layers (Fig. 3a and b). We refer to the formation of surface copper oxides on the core metallic Cu during the EA process of TT-CP as an "anomalous reduction" (Fig. 3c), contrasting with a typical reduction to

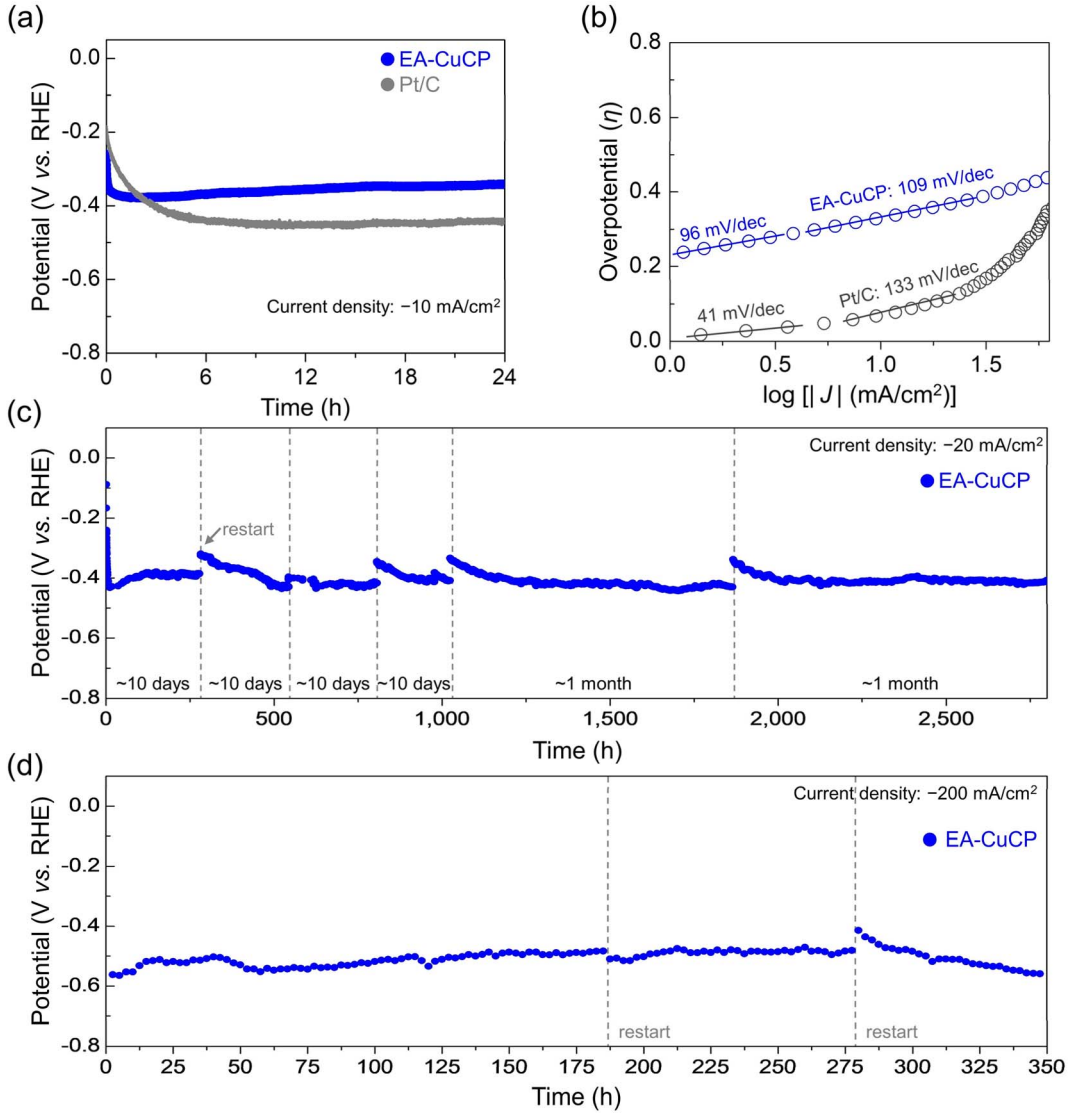

Fig. 2 HER durability of EA-CuCP compared to Pt/C. (a) Comparison of HER stability during one day between Pt/C and EA-CuCP. (b) Comparison of Tafel slopes between Pt/C and EA-CuCP. (c) Long-term HER stability test of EA-CuCP at the current density of −20 mA cm^{-2}. (d) Long-term HER stability measurement of EA-CuCP at the current density of −200 mA cm^{-2} operated over 350 h.

metallic Cu. HR-TEM image (Fig. 3d) and EDS line profile (Fig. S13, ESI†) of EA-CuCP reveal that the core metallic Cu shows (111) orientation toward surface facets and is capped by the surface layer of copper oxide nanoparticles, approximately 5 nm thick.

Spectroscopic analysis further supports the composite structure of EA-CuCP, where surface copper oxides cover core metallic Cu. The magnified Raman spectrum of EA-CuCP (Fig. S14, ESI†) shows well-defined vibrational modes of Cu_2O (T_{1u} and $2E_u$) and CuO (A_g and B_g). EA-CuCP exhibits a relatively high T_{1u} intensity, suggesting a Cu-deficient feature in Cu_2O and a peak shift in A_g (284 cm^{-1}) compared to CA-CuCP and TA-CuCP (297 cm^{-1}, Fig. S9, ESI†) originating from CuO nanoparticles (Fig. S14, ESI†).[38,39] The Cu 2p XPS spectrum of EA-CuCP also confirms the coexistence of Cu_2O and CuO on the surface (Fig. S15, ESI†). Additionally, the O 1s and C 1s XPS spectra exhibit signals of the Nafion binder and H_2SO_4 electrolyte originating from the EA process of TT-CP.[40,41] Similarly, the near edge X-ray absorption fine structure (NEXAFS) spectra of EA-CuCP in Cu L-edge measured by total electron yield (TEY) and total fluorescence yield (TFY) detection modes (Fig. S16, ESI†) identify a hierarchical copper-based composite structure with Cu_2O/CuO on the surface and core metallic Cu inside.

The fast Fourier transform (FFT) pattern taken from the local area of Fig. 3d, covering facet-1, confirms that the surface copper oxides are Cu_2O and CuO (Fig. 3e). Furthermore, the (111) orientation of Cu_2O nearly aligns with the (111) orientation of core metallic Cu (red arrow in Fig. 3e), while the (111) orientation of CuO is slightly distorted. Similar to facet-1, the core metallic Cu along facet-2 also shows the (111) orientation, with a similar alignment between the surface copper oxides and (111)-Cu (see Fig. S17, ESI†). We propose that surface copper

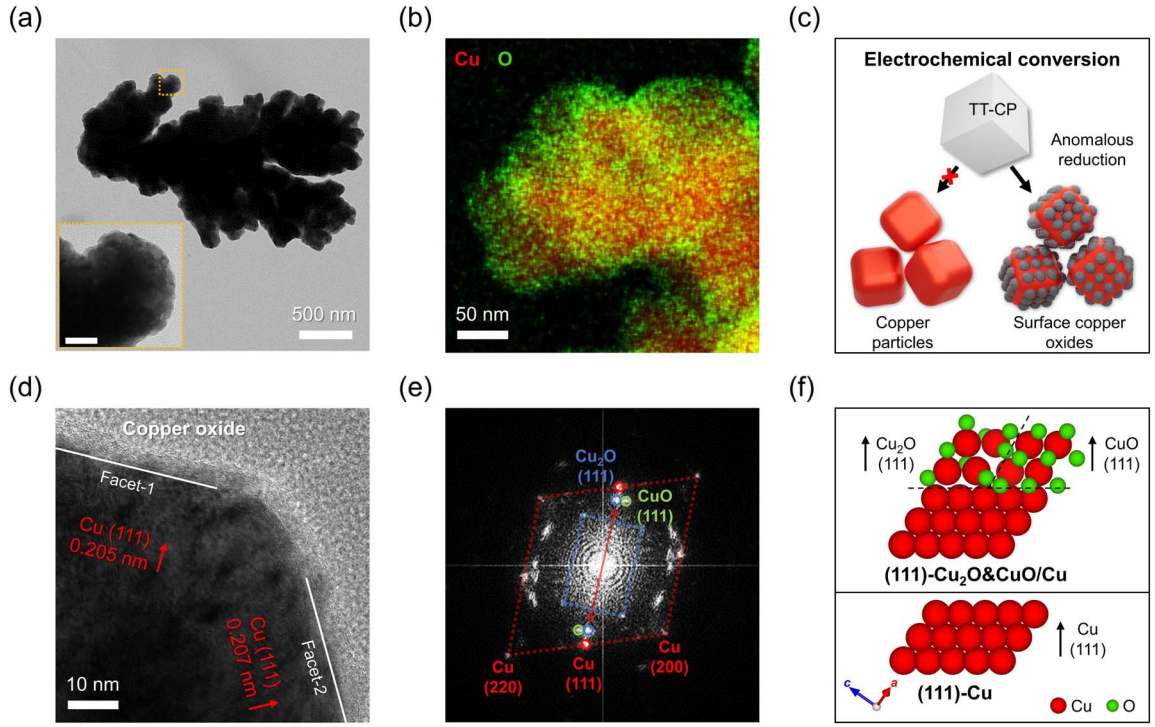

Fig. 3 Morphological investigation into the composite structure of EA-CuCP. (a) TEM image showing the overall morphology of EA-CuCP with an inset image revealing a magnified copper particle (inset scale bar: 50 nm). (b) Elemental mapping result of EA-CuCP. (c) Diagram expressing an anomalous reduction phenomenon by the electrochemical conversion from TT-CP to EA-CuCP. (d) HR-TEM image of EA-CuCP spotlighting the boundary between (111)-oriented Cu and copper oxides. (e) FFT pattern of EA-CuCP reflecting the local boundary structure of Cu, Cu_2O, and CuO, which visualizes the alignment along the Cu (111) direction. (f) Schematic illustration showing (111)-Cu and (111)-Cu_2O&CuO/Cu structures.

oxides (Cu_2O and CuO) form on the (111) surface of Cu during the EA process, unlike typical native oxides, which are generally over 10 nm thick and randomly oriented relative to core Cu.[42,43] In the EA-CuCP structure, core Cu and surface oxides maintain precise alignment, even in areas where core Cu transitions from the (200) to (111) orientation closer to the surface (shown in Fig. S18, ESI†). This unique copper-based composite structure in EA-CuCP, where surface Cu_2O and CuO align with the core Cu's (111) orientation, can be referred to as (111)-Cu_2O&CuO/Cu (Fig. 3f). Such specific alignment between copper and its surface oxides is not spontaneously formed in typical native oxides and is likely formed through the EA process of TT-CP. Furthermore, the three-phase contact among Cu, Cu_2O, and CuO—challenging to achieve under conventional oxidizing and reducing conditions[44,45]—was confirmed by inverse FFT patterns of EA-CuCP, which show Cu_2O and CuO layered within the surface oxide (see Fig. S19, ESI†). This unique (111)-Cu_2O&CuO/Cu structure, developed through the EA process, is highly likely to contribute to the excellent HER stability of EA-CuCP.

Structural stability and reduction resistance of EA-CuCP under HER conditions

To explain the excellent long-term HER stability of EA-CuCP in terms of reduction resistance of copper oxides, we investigated the structural change of EA-CuCP under different current conditions using *in situ* Raman spectroscopy, alongside commercial copper oxides such as Cu_2O (Com-Cu_2O) and CuO (Com-CuO). These commercial copper oxides were chosen to compare with the *in situ* developed copper oxide on the EA-CuCP surface. First, the HER performances of Com-Cu_2O and Com-CuO were evaluated (Fig. 4a). They exhibited higher overpotentials of 521 and 614 mV, respectively, compared to the EA-CuCP (331 mV). Additionally, the Tafel slopes of Com-Cu_2O (262 mV dec^{-1}) and Com-CuO (159 mV dec^{-1}) were higher than that of EA-CuCP (109 mV dec^{-1}), as shown in Fig. 1c and S20 (ESI).† This suggests that the HER kinetics of Cu_2O and CuO are less favorable and confirms that the increase in HER activity of EA-CuCP after electrochemical activation is not simply due to the formation of copper oxides.

In situ Raman measurements were conducted to investigate the structural stability of EA-CuCP under HER conditions compared to the Com-Cu_2O and Com-CuO (Fig. 4b). Initially, Com-CuO showed only CuO vibrational modes under no current applied. Under a current density of -10 mA cm^{-2}, the coexistence of Cu_2O and CuO appears, resulting from the reducing cathodic currents. At a current density of -20 mA cm^{-2}, Cu_2O and CuO signals were barely detected, indicating sequential reduction to Cu_2O and Cu. Similarly, Com-Cu_2O, with no current applied, showed both Cu_2O and CuO Raman signals. This observation is consistent with the Cu L-edge NEXAFS spectra of Com-Cu_2O and Com-CuO measured by bulk-sensitive TFY and surface-sensitive TEY modes (Fig. S16, ESI†). The surface structure of Com-Cu_2O was confirmed to

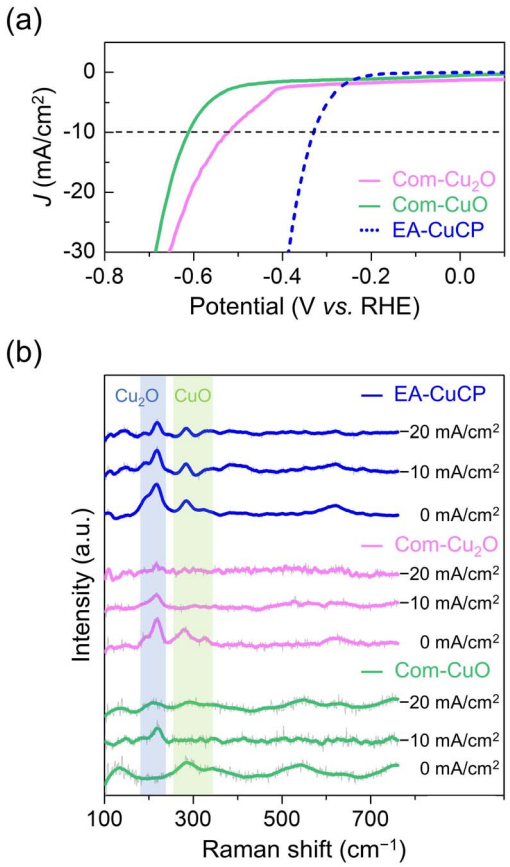

Fig. 4 Structural stability of EA-CuCP compared to commercial copper oxides. (a) HER polarization curves of Com-Cu_2O and Com-CuO. (b) *In situ* Raman spectra of Com-Cu_2O, Com-CuO, and EA-CuCP under the current densities of 0, −10, and −20 mA cm^{-2}.

consist of Cu_2O and CuO. Under the current densities of −10 and −20 mA cm^{-2}, the CuO signals nearly disappeared, and the Cu_2O signals weakened due to the instability of copper-oxide materials under HER conditions. This behavior is consistent with previous findings that single copper oxide components, such as Cu_2O and CuO, are generally unstable in acidic electrolytes under oxidation (to Cu^{2+}) and reduction (to Cu^0) conditions.[31] In addition, SEM analysis of EA-CuCP after the 2800 hours stability test revealed that the catalyst became aggregation, leading to an increase in particle size, similar to other catalysts. However, XPS confirmed that the hetero-valent (Cu^{2+}/Cu^+/Cu^0) composite structure, which is the origin of the stability of the catalyst, was preserved (Fig. S21 and S22, ESI†). Similarly, XRD data obtained from a two-week stability test showed the presence of copper signal in the catalyst, showing similarity to its state before the reaction (Fig. S23, ESI†). Notably, the EA-CuCP catalyst shows structural stability, maintaining its hetero-valent Cu_2O&CuO structure even after applying cathodic current densities. These *in situ* Raman measurements confirm the stability of the copper-based composite structure of EA-CuCP under reduction conditions during HER operation and suggest that the long-term stability is attributed to its hierarchical copper-based composite structure [(111)-Cu_2O&CuO/Cu] rather than a simple surface copper oxide.

Structure–property relationship of EA-CuCP

The Cu L-edge NEXAFS and Raman spectra of commercial copper-based materials (Fig. S24 and S25, ESI†) reveal that Cu foil and CuNP possess surface copper oxides, specifically Cu_2O and CuO, similar to those observed on the surface of EA-CuCP. However, their HER activity and stability are obviously different from those of EA-CuCP (Fig. 1b and c). Compared to the Cu foil and CuNP, EA-CuCP shows a stronger Cu_2O signal at 934.0 eV than the CuO signal at 930.6 eV. Additionally, EA-CuCP exhibits a distinct, aligned Cu^{2+}/Cu^+/Cu^0 structure (Fig. 3f), contrasting with the randomly oriented native oxides found on Cu foil and CuNP. This structural feature of EA-CuCP appears crucial, as the native oxides on Cu foil and CuNP do not similarly enhance HER activity and stability. Furthermore, all tested copper oxides, including TT-CP-derived materials (CA-CuCP and TA-CuCP) and commercial materials (Com-Cu_2O and Com-CuO), show poor HER kinetics and stability (Fig. 1 and 4). These comparisons indicate that the formation of aligned hetero-valent active sites (Cu^{2+}/Cu^+/Cu^0) in EA-CuCP supports its exceptional long-term HER stability.

The unique EA-CuCP structure, shown to contain (111)-oriented Cu_2O/Cu and CuO/Cu with a thin layer of Cu_2O or CuO, enhances H adsorption ability[46,47] and H_2O adsorption behavior.[48] The (111) alignment among Cu, Cu_2O, and CuO enables effective charge transport by promoting epitaxial pathways and facilitating shifts in the oxidation state from Cu^0 to Cu^+ and Cu^{2+}.[49] Coverage of core metallic Cu by (111)-Cu_2O&CuO significantly reduces charge transfer resistance (Fig. S26, ESI†), reducing OH^- and SO_4^- mediated reduction processes and improving electron transfer rates in the Cu_2O and CuO structures (Fig. 1c).

Cu coordination environment and anomalous reduction

To the best of our knowledge, the formation of hetero-valent copper through such an anomalous reduction process has not been previously reported. We hypothesize that the Cu coordination environment of the CP precursor plays a critical role in determining the unique structure of EA-CuCP. To test this, we modified the Cu-to-S ratio in TT-CP by adjusting the $CuCl_2$ content during synthesis (Fig. S27, ESI†). A modified TT-CP with a Cu to S ratio of 1 : 1 (TT-CP-mod) was activated to a catalyst without surface oxides (EA-CuCP-mod), as shown in Fig. 5a, which exhibited an overpotential of 626 mV at 10 mA (Fig. 5b), similar to typical copper-based materials.[50] Surface analysis revealed the absence of the Cu_2O and CuO, indicating that this TT-CP-mod precursor was fully reduced to metallic Cu during the EA process, unlike EA-CuCP synthesized from TT-CP with a Cu-to-S ratio of 1 : 1.5 (Fig. 5a). This result suggests that a sulfur-rich Cu coordination environment of TT-CP influences the copper oxide formation on the metallic Cu during activation, thereby contributing to outstanding HER stability, as revealed. As observed in other CP-derived and copper sulfide-derived Cu materials,[24,51] the metallic Cu core likely retains

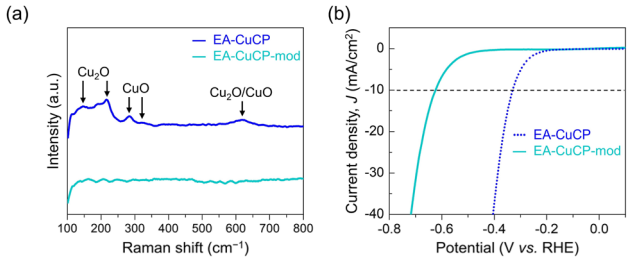

Fig. 5 Investigating the formation of surface oxides according to the Cu coordination environment of CPs. (a) Raman spectra of EA-CuCP and EA-CuCP-mod with controlled ratios of Cu and S. (b) HER polarization curve of EA-CuCP-mod compared to the EA-CuCP.

adsorbed sulfur atoms on its surface. These sulfur atoms are gradually replaced by H and H_2O species during the process, resulting in the formation of copper oxides. Thus, the TT-CP coordination environment is essential for generating hetero-valent copper in this catalyst development process.

Conclusions

In this work, we developed a highly stable copper-based HER catalyst with a unique hetero-valent ($Cu^{2+}/Cu^{+}/Cu^{0}$) composite structure formed through electrochemical activation of TT-CP. Systematic investigations revealed that the (111)-aligned metallic Cu core and surface Cu_2O and CuO layers are uniquely formed through electrochemical activation, unlike those produced by annealing or chemical methods. Notably, the catalyst exhibited exceptional long-term stability, maintaining performance for over 2800 h (~3 months) with an overpotential of 407 mV at −20 mA cm^{-2}. This durability is attributed to the Cu_2O&CuO/Cu structure, which enhances hydrogen adsorption and reduces charge transfer resistance due to its aligned hetero-valent properties. *In situ* Raman comparisons with copper references confirmed that the stability is not merely a result of surface copper oxides. Instead, the enhanced stability arises from the formation of hetero-valent copper oxides under electrochemical reduction conditions, which are possible by the sulfur-rich Cu coordination environment of TT-CP. This finding demonstrates the potential of copper-based materials as robust and cost-effective alternatives to noble metal catalysts in HER, offering promising pathways for sustainable, long-term solutions in electrocatalysis.

Data availability

The data supporting this article have been included as part of the ESI.†

Author contributions

Taehun Im: investigation, methodology, visualization, writing – original draft. Joo-Won Lee: conceptualization, formal analysis, investigation, writing – original draft. Sung-Chul Kim: formal analysis, investigation. SungJu Jun: investigation Jae-Seung Lee: validation, resources. Min-Seok Kim: validation, resources. Jae Kyun Lee: formal analysis, investigation, resources. Sohee Jeong: conceptualization, funding acquisition, writing – review & editing, project administration.

Conflicts of interest

There are no conflicts to declare.

Acknowledgements

This research was supported by the Pioneer Research Center Program (RS-2024-00431320) and the Future Hydrogen Original Technology Development Program (NRF-2021M3I3A1083946) through the National Research Foundation of Korea (NRF) funded by the Korean government (Ministry of Science and ICT) and the Future Key Technology Program (Project No. 2E33241) funded by the Korea Institute of Science and Technology.

Notes and references

1 J. Greeley, T. F. Jaramillo, J. Bonde, I. Chorkendorff and J. K. Nørskov, *Nat. Mater.*, 2006, **5**, 909–913.
2 X. Liu, G. Chen, Y. Guo, T. Li, J. Huang, W. Chen and K. K. Ostrikov, *J. Colloid Interface Sci.*, 2024, **659**, 895–904.
3 H. Yan, Y. Wang, Y. Xin, Z. Jiang, B. Deng and Z. J. Jiang, *Small*, 2024, **20**, 2406070.
4 D. Hu, Y. Wang, W. Chen, Z. Jiang, B. Deng and Z. J. Jiang, *Small*, 2024, **20**, 2402652.
5 I. Roger, M. A. Shipman and M. D. Symes, *Nat. Rev. Chem.*, 2017, **1**, 0003.
6 P. Yu, F. Wang, T. A. Shifa, X. Zhan, X. Lou, F. Xia and J. He, *Nano Energy*, 2019, **58**, 244–276.
7 G. Chen, H. Xiang, Y. Guo, J. Huang, W. Chen, Z. Chen, T. Li and K. K. Ostrikov, *Carbon Energy*, 2024, **6**, e522.
8 P. Wang, S. Meng, B. Zhang, M. He, P. Li, C. Yang, G. Li and Z. Li, *J. Am. Chem. Soc.*, 2023, **145**, 26133–26143.
9 R. Amirbeigiarab, J. Tian, A. Herzog, C. Qiu, A. Bergmann, B. R. Cuenya and O. M. Magnussen, *Nat. Catal.*, 2023, **6**, 837–846.
10 Q. Chang, J. H. Lee, Y. Liu, Z. Xie, S. Hwang, N. S. Marinkovic, A.-H. A. Park, S. Kattel and J. G. Chen, *JACS Au*, 2022, **2**, 214–222.
11 L. Pan, Y. Liu, L. Yao, D. Ren, K. Sivula, M. Grätzel and A. Hagfeldt, *Nat. Commun.*, 2020, **11**, 318.
12 D. Jeong, W. Jo, J. Jeong, T. Kim, S. Han, M.-K. Son and H. Jung, *RSC Adv.*, 2022, **12**, 2632–2640.
13 L. Pan, J. H. Kim, M. T. Mayer, M.-K. Son, A. Ummadisingu, J. S. Lee, A. Hagfeldt, J. Luo and M. Grätzel, *Nat. Catal.*, 2018, **1**, 412–420.
14 K. Kannimuthu, K. Sangeetha, S. S. Sankar, A. Karmakar, R. Madhu and S. Kundu, *Inorg. Chem. Front.*, 2021, **8**, 234–272.
15 W.-J. Kang, Y. Feng, Z. Li, W.-Q. Yang, C.-Q. Cheng, Z.-Z. Shi, P.-F. Yin, G.-R. Shen, J. Yang, C.-K. Dong, H. Liu, F.-X. Ye and X.-W. Du, *Adv. Funct. Mater.*, 2022, **32**, 2112367.

16 H. Huang, H. Jung, S. Li, S. Kim, J. W. Han and J. Lee, *Nano Energy*, 2022, **92**, 106763.
17 L. Ye and Z. Wen, *Chem. Commun.*, 2018, **54**, 6388–6391.
18 S. Czioska, J. Wang, X. Teng and Z. Chen, *ACS Sustainable Chem. Eng.*, 2018, **6**, 11877–11883.
19 J. Tian, Q. Liu, N. Cheng, A. M. Asiri and X. Sun, *Angew. Chem., Int. Ed.*, 2014, **53**, 9577–9581.
20 C. Liu, X.-D. Zhang, J.-M. Huang, M.-X. Guan, M. Xu and Z.-Y. Gu, *ACS Catal.*, 2022, **12**, 15230–15240.
21 Y. Zhang, Y. Chen, X. Wang, Y. Feng, Z. Dai, M. Cheng and G. Zhang, *Nat. Commun.*, 2024, **15**, 5172.
22 X. Wang, K. Klingan, M. Klingenhof, T. Möller, J. F. de Araújo, I. Martens, A. Bagger, S. Jiang, J. Rossmeisl, H. Dau and P. Strasser, *Nat. Commun.*, 2021, **12**, 794.
23 W. Zhai, Y. Ma, D. Chen, J. C. Ho, Z. Dai and Y. Qu, *InfoMat*, 2022, **4**, e12357.
24 C. Liang, X. Li, J. Han, N. Ye, H. Liu, H. Feng, L. Huang, Y. Liu and X. Peng, *J. Alloys Compd.*, 2021, **883**, 160816.
25 X.-D. Zhang, T. Liu, C. Liu, D.-S. Zheng, J.-M. Huang, Q.-W. Liu, W.-W. Yuan, Y. Yin, L.-R. Huang, M. Xu, Y. Li and Z.-Y. Gu, *J. Am. Chem. Soc.*, 2023, **145**, 2195–2206.
26 J.-D. Yi, R. Xie, Z.-L. Xie, G.-L. Chai, T.-F. Liu, R.-P. Chen, Y.-B. Huang and R. Cao, *Angew. Chem., Int. Ed.*, 2020, **132**, 23849–23856.
27 H. Huo, J. Wang, Q. Fan, Y. Hu and J. Yang, *Adv. Energy Mater.*, 2021, **11**, 2102447.
28 S. Bahçeli, E. K. Sarıkaya, Ö. Dereli and F. P. Özturan, *J. Mol. Struct.*, 2020, **1216**, 128315.
29 T. Im, J. Lee, S.-C. Kim, J. Randrianandraina, J.-W. Lee, M. W. Chung, T. Park, K.-H. Low, S. Lee, S. J. Oh, Y. C. Kang, S. Weon, J.-H. Lee, S. J. Kim and S. Jeong, *Mater. Horiz.*, 2024, **11**, 4970–4978.
30 S. Liu, Y. Lei, Z. Yang and Y. Lan, *J. Mol. Struct.*, 2014, **1074**, 527–533.
31 B. Beverskog and I. Puigdomenech, *J. Electrochem. Soc.*, 1997, **144**, 3476.
32 H. Prats and K. Chan, *Phys. Chem. Chem. Phys.*, 2021, **23**, 27150–27158.
33 H. Wei, K. Huang, D. Wang, R. Zhang, B. Ge, J. Ma, B. Wen, S. Zhang, Q. Li, M. Lei, C. Zhang, J. Irawan, L.-M. Liu and H. Wu, *Nat. Commun.*, 2017, **8**, 1490.
34 X. Cheng, Y. Li, L. Zheng, Y. Yan, Y. Zhang, G. Chen, S. Sun and J. Zhang, *Energy Environ. Sci.*, 2017, **10**, 2450–2458.
35 Z. Pu, I. S. Amiinu, Z. Kou, W. Li and S. Mu, *Angew. Chem., Int. Ed.*, 2017, **56**, 11559–11564.
36 R. T. Gao, N. T. Nguyen, T. Nakajima, J. L. He, X. H. Liu, X. Y. Zhang, L. Wang and L. M. Wu, *Sci. Adv.*, 2023, **9**, eade4589.
37 P. Wang, C.-H. Gong, A.-Y. Tang, A.-T. Gu, K.-W. Chen and Y. Yi, *Mater. Res. Express*, 2023, **10**, 025005.
38 C. V. Kartha, J.-L. Rehspringer, D. Muller, S. Roques, J. Bartringer, G. Ferblantier, A. Slaoui and T. Fix, *Ceram. Int.*, 2022, **48**, 15274–15281.
39 J. F. Xu, W. Ji, Z. X. Shen, W. S. Li, S. H. Tang, X. R. Ye, D. Z. Jia and X. Q. Xin, *J. Raman Spectrosc.*, 1999, **30**, 413–415.
40 B. Tazi and O. Savadogo, *Electrochim. Acta*, 2000, **45**, 4329–4339.
41 M. Wahlqvist and A. Shchukarev, *J. Electron Spectrosc. Relat. Phenom.*, 2007, **156–158**, 310–314.
42 Y. S. Chu, I. K. Robinson and A. A. Gewirth, *J. Chem. Phys.*, 1999, **110**, 5952–5959.
43 J. Iijima, J.-W. Lim, S.-H. Hong, S. Suzuki, K. Mimura and M. Isshiki, *Appl. Surf. Sci.*, 2006, **253**, 2825–2829.
44 D. Mahana, A. K. Mauraya, P. Singh and S. K. Muthusamy, *Solid State Commun.*, 2023, **366–367**, 115152.
45 J. Y. Kim, J. A. Rodriguez, J. C. Hanson, A. I. Frenkel and P. L. Lee, *J. Am. Chem. Soc.*, 2003, **125**, 10684–10692.
46 Z. Riguang, L. Hongyan, L. Lixia, L. Zhong and W. Baojun, *Appl. Surf. Sci.*, 2011, **257**, 4232–4238.
47 J. Zhang, R. Zhang, B. Wang and L. Ling, *Appl. Surf. Sci.*, 2016, **364**, 758–768.
48 F. Chiter, D. Costa, V. Maurice and P. Marcus, *J. Phys. Chem. C*, 2020, **124**, 17048–17057.
49 A. Dey, G. Chandrabose, L. A. O. Damptey, E. S. Erakulan, R. Thapa, S. Zhuk, G. K. Dalapati, S. Ramakrishna, N. S. J. Braithwaite, A. Shirzadi and S. Krishnamurthy, *Appl. Surf. Sci.*, 2021, **541**, 148571.
50 P. Farinazzo Bergamo Dias Martins, P. Papa Lopes, E. A. Ticianelli, V. R. Stamenkovic, N. M. Markovic and D. Strmcnik, *Electrochem. Commun.*, 2019, **100**, 30–33.
51 T. Shinagawa, G. O. Larrazábal, A. J. Martín, F. Krumeich and J. Pérez-Ramírez, *ACS Catal.*, 2018, **8**, 837–844.